

## REVIEW ARTICLE

# The promise and the challenges of cryo-electron tomography

Martin Turk  and Wolfgang Baumeister 

Department of Molecular Structural Biology, Max Planck Institute of Biochemistry, Martinsried, Germany

**Correspondence**

W. Baumeister, Department of Molecular Structural Biology, Max Planck Institute of Biochemistry, Am Klopferspitz 18, D-82152 Martinsried (Planegg), Germany  
Tel: 49 (89) 8578-2642  
E-mail: baumeist@biochem.mpg.de

(Received 17 June 2020, revised 28 September 2020, accepted 28 September 2020, available online 23 October 2020)

[Correction added on 24 November 2020, after first online publication: Projekt Deal funding statement has been added.]

doi:10.1002/1873-3468.13948

Edited by John Briggs

**Structural biologists have traditionally approached cellular complexity in a reductionist manner in which the cellular molecular components are fractionated and purified before being studied individually. This ‘divide and conquer’ approach has been highly successful. However, awareness has grown in recent years that biological functions can rarely be attributed to individual macromolecules. Most cellular functions arise from their concerted action, and there is thus a need for methods enabling structural studies performed *in situ*, ideally in unperturbed cellular environments. Cryo-electron tomography (Cryo-ET) combines the power of 3D molecular-level imaging with the best structural preservation that is physically possible to achieve. Thus, it has a unique potential to reveal the supramolecular architecture or ‘molecular sociology’ of cells and to discover the unexpected. Here, we review state-of-the-art Cryo-ET workflows, provide examples of biological applications, and discuss what is needed to realize the full potential of Cryo-ET.**

**Keywords:** cellular structural biology; correlative light-electron microscopy; cryo-electron tomography; image processing workflow; sample preparation workflows; structural biology *in situ*

A comprehensive understanding of the inner workings of cells needs more than knowledge of their molecular inventories or the sum of individual molecular structures [1,2]. When cells are taken apart and molecules are released from their functional environment, all information about their interactions and context is irrecoverably lost. It is common belief now that cellular functions are not the result of random collisions of individual molecules; they rather require the concerted actions of functional modules [3,4]. Many of these exist only transiently, while others, being more stable, may be so deeply rooted in their cellular environment that they cannot be isolated without violation of their structural integrity. Hence, there is a compelling need for methods that

allow visualizing the molecular architecture of cells *in situ* [5].

There is no single method that could give us the whole picture; it rather requires an ‘imaging across scales’ approach and the integration of data covering different length scales (Fig. 1). At one end of the spectrum are the methods providing high-resolution structures of isolated and purified molecules, such as X-ray crystallography, nuclear magnetic resonance spectroscopy (NMR), and cryo-electron microscopy (cryo-EM) single-particle analysis. In recent years, the latter method has emerged as the most versatile method unrivalled in particular when it comes to large and flexible macromolecular assemblies [6]. At the other end of the spectrum are methods allowing the

**Abbreviations**

CLEM, Correlative light-electron microscopy; Cryo-EM, Cryo-electron microscopy; Cryo-ET, Cryo-electron tomography; Cryo-FM, Cryo-fluorescence light microscopy; CTF, Contrast transfer function; FIB, Focused-ion beam; FIB-SEM, Ion-beam block face scanning electron microscopy; TEM, Transmission electron microscope; VPP, Volta phase plate; ZPP, Zernike phase plate.

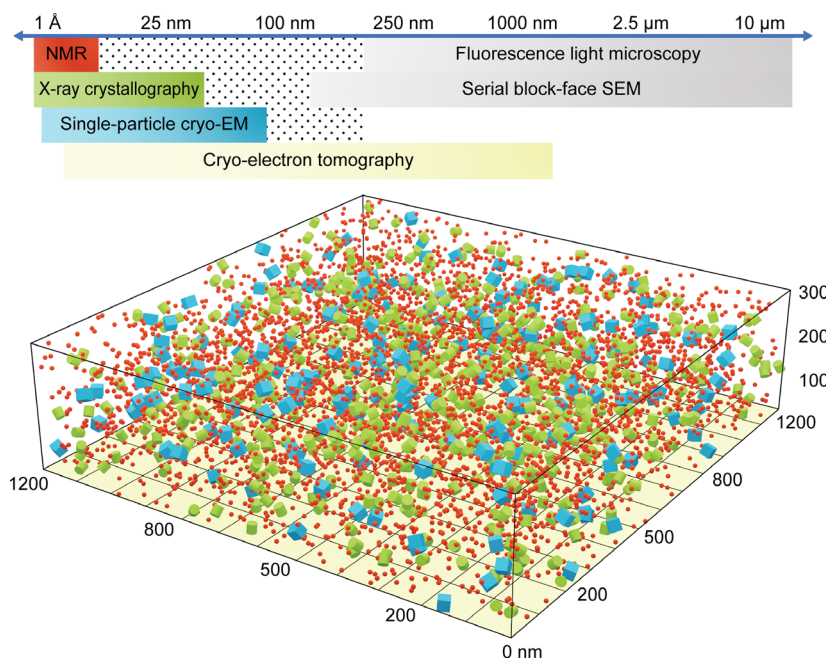


**Fig. 1.** Imaging across scales aims at a detailed and comprehensive description of the cellular space. This can be achieved by the integration of high-resolution structures into large volume data. *In situ* cryo-ET provides a crucial link by bridging the resolution gap (dotted region) between *ex situ* high-resolution structures and low-resolution large volume data. Boxes of the structural methods below the scale bar indicate the attainable resolutions (left) and scales over which information can be obtained (right). The volume of the box corresponds to a typical volume of a single tomogram. It is populated with imaginary particles of sizes typical for the various high-resolution methods (red NMR, green X-ray crystallography, blue single-particle analysis). In this scheme, the occupancy of the cellular space is underrepresented (2,3%). In reality, cells are much more crowded (occupancy 20–30% of the volume).

visualization of whole cells and their dynamics such as super-resolution light microscopy. When combined with ion-beam block face scanning electron microscopy (FIB-SEM), striking multimodal views of large volumes can be obtained [7]. Cryo-electron tomography (cryo-ET) provides a crucial link between whole-cell imaging and high-resolution structure determination. It provides molecular resolution 3D images of cellular landscapes, but is restricted in volume because larger samples must be thinned to  $< 1 \mu\text{m}$  to render them electron transparent [8]. Otherwise, the only preparation step is vitrification by rapid freezing, yielding pristinely preserved samples. Chemical fixation and staining which bear the risk of altering the macromolecular organization of cells are avoided altogether.

## Workflow

### Sample preparation

Small objects such as viruses [9–12], isolated organelles [13], cell appendages [14–16], small bacteria [17], or minicells [18] can be studied *in toto*. For cellular structural studies, cells are grown on grids which must be

non-cytotoxic. To have some control over where cells grow, avoiding, for example, areas obstructed by grid bars, micropatterning methods can be used [19] (Fig. 2). Vitrification of single cells not exceeding a thickness of  $\sim 5 \mu\text{m}$  can be achieved by plunge freezing [20]. For thicker objects, high-pressure freezing is indispensable to avoid ice-crystal formation and its deleterious consequences for cellular ultrastructure [21,22].

After vitrification most cells require thinning to render them electron transparent. Serial sections can be cut with a cryo-microtome, but compression artifacts and poor reproducibility have limited the use of this method [23]. Focused-ion beam (FIB)-milling has become the method of choice for compression-free specimen thinning [24,25]. By controlling the stream of  $\text{Ga}^+$  ions, different thinning geometries (lamellae, wedges) can be realized. In combination with cryo-compatible micromanipulators, slabs of high-pressure frozen samples can be lifted out and placed on EM grids for further thinning. This cryo-FIB lift-out method expands the range of samples that can be studied by cryo-ET to eukaryotic cells, multicellular organisms, and tissues [26].

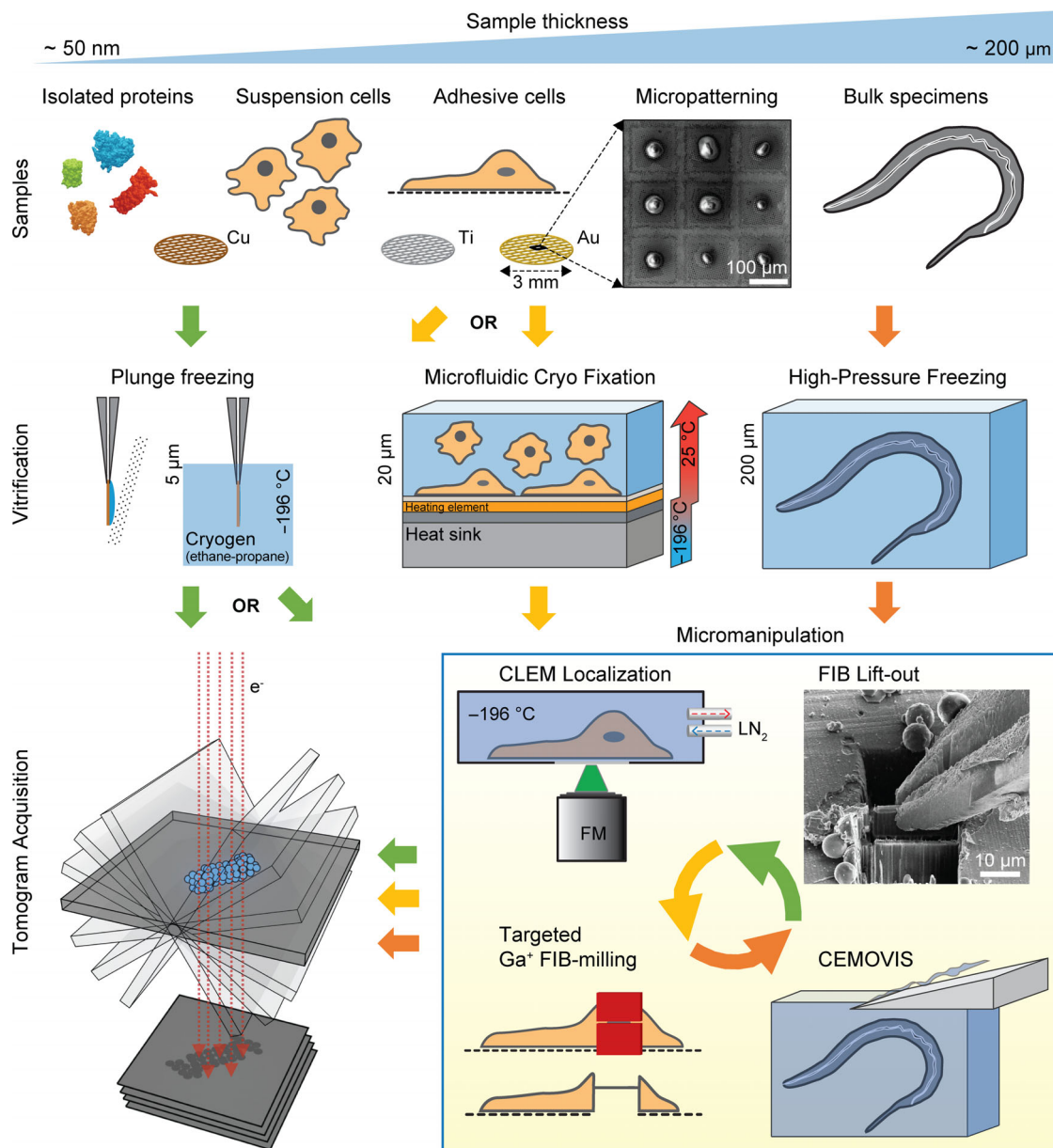


**Fig. 2.** Cryo-ET workflow from sample preparation to tomogram acquisition. Sample thickness determines the vitrification method and the subsequent processing steps, producing samples with thicknesses (< 0.5 µm) allowing electron imaging. Cryo-ET can be applied to a broad range of samples from isolated macromolecules to multicellular organisms. Arrows indicate possible workflow directions for different sample groups. For adhesive cells, the use of lasers for drawing patterns (micropatterning) provides control over where cells attach and can induce different morphologies. Vitrification is mostly achieved under atmospheric pressure either by plunge freezing, where samples are applied to EM grids, blotted, and plunged into a cryogen kept close to -196 °C, or microfluidic vitrification, where a rapid temperature drop is achieved by switching off the heater element between the sample and the heat sink. Thicker specimens need to be vitrified by high-pressure freezing (2045 bar) and may need the addition of cryoprotectants. Micromanipulation (box) includes optional steps that can be combined depending on experimental requirements. CLEM utilizes cryo-FM to identify regions of interest and enables targeted thinning of samples using FIB-milling. Cryo-FIB lift-out allows examining parts of bulky specimens. Cryo-electron microscopy of vitreous sections (CEMOVIS) can be used for initial trimming of bulky specimens. Finally, specimens are imaged using an electron beam in a fashion similar to computer-aided tomography. The main difference is that projections of different views are obtained by rotating the sample in the beam instead of rotating the beam around the sample.

Correlative light-electron microscopy (CLEM) allows for the identification and localization of features or events of interest in large cellular landscapes, and their precise targeting for FIB-milling [27–30]. Cryogenic super-resolution optical fluctuation imaging (cryo-SOFI) further improves the localization precision of fluorescently labeled proteins beyond the diffraction limit [31]. However, the signal localization precision of live cell imaging suffers from a time delay, between imaging and vitrification, on the scale of seconds. Recently, microfluidics cryofixation devices have been used to address this issue. They are able to arrest a particular cellular state within milliseconds by enabling vitrification on the imaging stage [32].

### Data acquisition

To obtain a tomogram of the area of interest a series of projection images is recorded, while tilting the sample in the microscope. After refining the eucentric height over the recording position, four steps need to be repeated for each tilt in the series: tilting, centering, focusing, and recording. The angular increments can be either equally spaced or closer together as the tilt angle increases [33]. The tilt series range is usually limited to  $\pm 60^\circ$ . Different mono- and bidirectional tilt schemes are used to distribute the electron dose in a preferred sequence. The now widely used dose-symmetric tilt scheme changes the tilt direction for every step, starting at  $0^\circ$  and climbing its way up to the maximum tilt [34,35]. The main advantage of starting data collection at low angles, where the path of the electrons through the sample is shortest, is the preservation of high-resolution information before the onset of serious radiation damage. In addition, almost symmetrical distribution of the electron dose minimizes alignment jumps notorious for bidirectional tilt schemes.

Because of the radiation sensitivity of frozen-hydrated biological material, the exposure to the electron beam must be minimized. Optimal exposure is dependent on both the sample sensitivity to ionizing radiation and the resolution aimed at. At exposures around  $160 \text{ e}\cdot\text{\AA}^{-2}$ , gas bubbles develop causing severe structural damage [36]. Distributing the total allowable electron dose over a tilt series leads to low signal-to-noise ratios (SNR) of the individual images. In addition, for higher tilt angles the path electrons traverse through the slab-shaped samples increases, resulting in multiple electron scattering further reducing the SNR. Moreover, obtaining views over the whole  $180^\circ$  angular range is not possible due to the physical design of the specimen holder that obstructs the beam path at

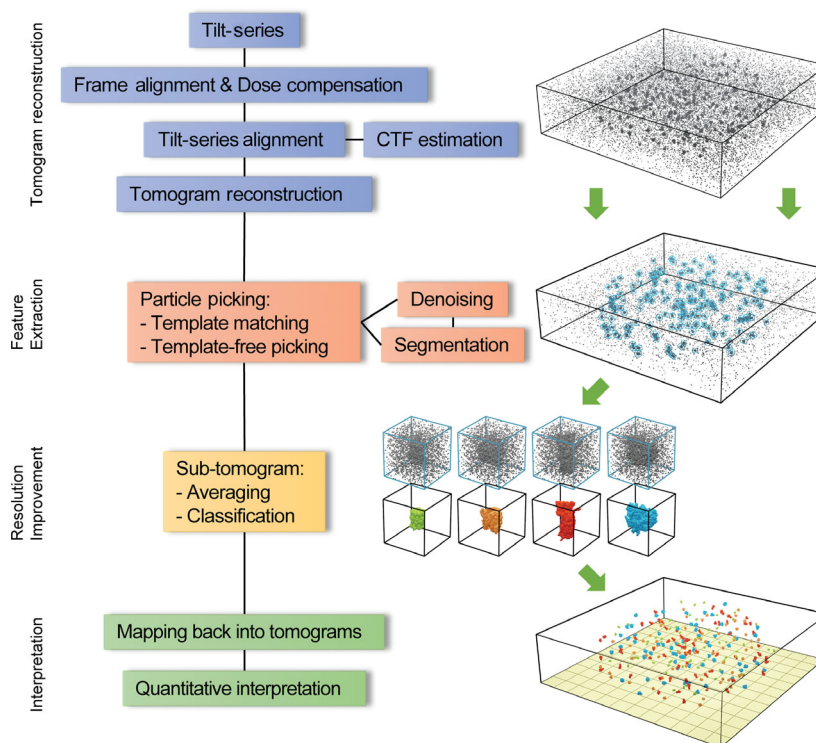
higher tilt angles. The limited angular sampling range of projections results in the ‘missing wedge’ of information in Fourier space that causes elongation artifacts in reconstructed tomograms parallel to the electron beam direction [37]. In transmission electron microscopes (TEM) with a dual-axis stage, a tilt series can be recorded in two directions, reducing the missing information to a missing pyramid yielding a more isotropic resolution [38].

An additional factor to consider when recording a tomogram is magnification, which determines the theoretically achievable maximum resolution according to the Nyquist–Shannon sampling theorem [39]. Here, one has to keep in mind that when magnification is increased the intensity of the beam needs to be increased as well, in order that the number of electrons per pixel stays the same and that frame and tilt series alignment are not compromised. Therefore, the electron exposure of the specimen, measured in electrons/ $\text{\AA}^2$ , increases quadratically with magnification; that is for a 2-fold increase in magnification, the electron exposure of the sample increases 4-fold. Selecting optimal recording parameters needs to reconcile the optimization of sampling with the need to limit the cumulative exposure.

### Tomogram reconstruction

The projection images are pre-processed and aligned before a tomogram is reconstructed. Nowadays, pre-processing benefits from the fast readout and improved SNR provided by direct electron detectors. Recording in movie mode allows the correction of beam-induced sample motions, which otherwise limit resolution [40], and it allows for low-pass filtering of movie frames in such a way that the filter cutoff is following the gradual demise of high-resolution structural information as the total exposure to the electron beam accumulates [41]. Recently, fiducial-based motion correction has been extended to the whole tilt series, reducing the effect of out-of-plane sample deformations during exposure [42]. Next, alignment of the tilt series brings the projections into a common register. The addition of nano-sized high-contrast fiducial markers to the samples, typically 5–20 nm gold beads, increases the alignment accuracy. The tilt series alignment of FIB-milled lamellae without fiducials requires patch tracking [43] or tracking of intrinsic high-contrast features [44]. The functionality for automated tracking and tilt series alignment as well as routines for tomogram reconstruction are integrated in, for example, the widely used IMOD software package [43] or in the Protomo implementation inside Appion [45]. For

**Fig. 3.** Tomogram reconstruction workflow. Projection images of a tilt series are aligned and back-projected into a tomographic volume. To facilitate particle picking, denoising filters can be applied and features, such as membranes, can be segmented to further constrain the search space. Resolution of the extracted sub-tomograms can be improved by averaging and classification methods. Finally, a tomographic model is generated by placing extracted objects back into their refined 3D orientations, enabling the analysis and quantitative interpretation of their spatial distribution in the context of the cellular environment.



sufficient levels of phase contrast for cryo-ET, a tilt series is conventionally acquired in underfocus. To successfully restore the high-resolution image information, it is necessary to accurately determine the defocus and correct for the contrast transfer function (CTF). The simplest approaches divide each tilt image into strips or patches and estimate the defocus gradient perpendicular to the tilt axis [46–48]. For sub-tomogram averaging more accurate 3D CTF correction methods consider also the particle height in the tomogram [49,50].

The aligned tilt series data are then computationally reconstructed into a tomogram (Fig. 3) by any of the available reconstruction methods. Most commonly, weighted back-projection (WBP) [51,52] is used for its speed and preservation of high-resolution information, although direct Fourier inversion methods have certain advantages [44]. Iterative reconstruction methods yield improved contrast compared to WBP [53] and have been shown to reduce the distortions caused by the ‘missing wedge’ [54–56]. These characteristics are useful for visual tomogram interpretation and for sub-tomogram alignment [53]; however, for sub-tomogram averaging, unlike WBP, high-frequency information may be lost [53]. Recently, improved iterative methods outperformed the WBP method in the 2–3 nm resolution range [56–58].

### Tomogram interpretation

Interpretation of structural features from reconstructed tomograms is especially challenging for crowded cellular systems and low SNR datasets. Denoising filters enhance structural features by suppressing noise, while preserving most of the signal. For example, non-linear anisotropic diffusion enhances edges [59,60], whereas more specialized filters are used to track filaments or to segment membranes [61,62]. Recently, convolutional neural networks have taken advantage of the fast detector readout to train a noise model on the basis of frames [63].

Denoising filters greatly facilitate segmentation. Image segmentation not only aids visual interpretation but also enables quantitative analysis, such as distance-based analysis of specific protein populations to segmented membranes [64,65]. Macromolecules can be located using templates derived from already known structures [66,67]. However, finding different molecular species in complex systems relies on the availability of large template libraries and the computationally demanding template search is usually limited to a few molecular species. Constraining the search space, where prior knowledge is available, can greatly facilitate the speed and accuracy of template matching. For example, the search space for membrane-embedded

molecular complexes can be constrained to segmented membranes. Several software packages augment the labor-intensive manual segmentation [68,69]. Convolutional neural networks can be trained on segmented data [70] or to extract features automatically, in an unsupervised fashion [71]. While automation reduces user bias and increases throughput, some manual intervention is still required to set boundary conditions.

To avoid bias and enable detection of novel complexes, it is desirable to develop methods that are not relying on predefined templates, but rather use the tomogram data for pattern mining. Recently, a template-free detection method was developed and successfully applied to membrane-bound complexes [72] and a multi-pattern pursuit method for automated detection of frequently occurring structural features in tomograms [73].

### Sub-tomogram averaging

When tomograms contain repetitive features, resolution can be improved by averaging multiple copies of structures of interest using methods akin to those being used in single-particle analysis. Extracted sub-tomograms are iteratively aligned and averaged to increase their SNR and resolution. For every iteration, the relative rotations and shifts between sub-tomograms and the reference structure are determined by a cross-correlation similarity metric [53]. Applying these orientations yields a new reference, which is used to refine the sub-tomogram orientations in the subsequent iteration round. Refinement is repeated until convergence or a specified iteration number has been reached. To avoid overfitting, the reference structure is filtered between iteration rounds to its estimated resolution by comparing resolution shells of two independently reconstructed volumes obtained by splitting the dataset into two halves [74]. In addition, maximum likelihood methods further reduce the risk of overfitting by allowing each sub-tomogram to simultaneously contribute to different orientations in a weighted manner [75]. To reduce the compositional and conformational heterogeneity and to further improve the averaging results, it is necessary to classify the sub-tomograms into more homogenous subsets. Different averaging and classification methods have co-evolved and among other features consider the missing wedge by performing constrained cross-correlations [67,76], provide speed improvements [77,78], and employ different classification strategies [72,79–81]. Instead of finding subpopulations by global comparison, masks can be applied to specific areas for focused classification. To reduce bias,

masks can be automatically generated from the local variance between sub-tomogram averages generated from subsets of the whole dataset [82]. In this way, different assembly, functional, and binding states of *in situ* 26S proteasomes have been successfully identified as well as two distinct oligomeric forms of tripeptidyl peptidase II [64,83,84].

Several software packages integrate various tools for sub-tomogram analysis; Dynamo [85], EMAN2 [86], emClarity [87], PEET [88], Protomo [89], PyTom [90], RELION [91]. These packages include functionalities for different sub-tomogram averaging steps; some provide also data management, allow users to design highly customizable workflows, or they guide sub-tomogram analysis along a predefined path. A comparison of their features can be found in Chen *et al.* [44].

### Examples

Cryo-ET has provided insights into the structure and function of viruses [9–12,92–97], nuclear pore complexes [64,98–100], ribosomes [101–103], coated vesicles [104–109], nucleosome arrangement in chromatin [110], cytoskeletal elements [111–113], bacterial secretion systems [114–117], chemotaxis [118,119], flagellar motors [120], and S-layers [121]. Obtaining information about the spatial arrangement of proteins by cryo-ET has also found use in assessing protein denaturation at the air-buffer interface for single-particle analysis [122]. To illustrate its broad applicability, examples are discussed that utilize different parts of the cryo-ET workflow, reveal insights at different length scales, and enable integration with other structural determination methods.

### Viruses and bacterial S-layers

Structural studies of viruses have been driving methods developments in 3D EM since the early days [123]. Sub-tomogram averaging has been used widely for studies of pleomorphic viruses. Examples include the murine leukemia retrovirus [92,93], rubella virus [94], herpes simplex virus type I [9,95], and the severe acute respiratory syndrome coronavirus 2 [96,97]. Sub-tomogram averaging of viral lattices with high local order resulted in the first sub-nanometer resolutions for the *ex situ* Ebola nuclear capsid [10] and fullerene-like HIV-1 capsid [11]. For the well-behaved immature HIV-1 capsid, near-atomic 3.9 Å resolution was achieved [12]. This was further improved to 3.4 Å by applying 3D CTF correction [50], and more recently to 3.1 Å with emClarity, a sub-tomogram averaging package [87]. In addition to sub-tomogram averaging

and data-collection advances, new insights into the assembly and maturation of viral capsids have been obtained.

Application of these developments has resulted in the first 4.8 Å *in situ* cryo-ET structure of *Caulobacter crescentus* surface layer [121] (Fig. 4A). S-layers are 2D arrays of proteins that provide protection and structural support to many bacteria and archaea. Using an integrative approach combining cryo-ET, single-particle averaging, and native mass spectrometry (MS), a high-resolution structural model of the S-layer was generated. This provided insights into the S-layer lattice organization, its interaction with surface lipopolysaccharides and dependence on calcium ions, and exemplifies the progress EM has made in the past three decades, since the first electron crystallography structure of *C. crescentus* S-layer [124].

## COPI

Coat protein complex I (COPI) has been extensively studied *ex situ* and *in situ*. COPI-coated vesicles transport cargo within the Golgi network and in the retrograde direction to the endoplasmic reticulum. These heteroheptameric complexes assemble on the surface of the *cis* Golgi cisternae where they are recruited by Arf1 to facilitate the formation of membrane buds for transport. Cryo-ET of *ex situ* assembled COPI vesicles from mouse proteins revealed flexibly linked trimeric assemblies as the basic modules covering the vesicle surface [104]. At 13 Å the basic molecular architecture of the COPI was established [105] (Fig. 4B). Taking advantage of improved data acquisition schemes and local alignment, resolution was further improved to 9 Å. This allowed refinement of the COPI architecture and provided insights into the coatomer formation and disassembly [106].

*In situ* studies by cryo-ET FIB-milled lamellae from *Chlamydomonas reinhardtii* provided the native COPI structure at 20 Å [107]. Comparison of the independently reconstructed *in situ* COPI structure showed high similarity to the *ex situ* COPI structure, confirming that reconstitution faithfully recapitulated the *in situ* scenario. In contrast to the empty *ex situ* vesicles, however, the luminal side of native COPI contained additional density indicating bound cargo or cargo receptors. Interpretation of the COPI in the context of their native environment provided insights into the COPI morphology and apparent half-life in the cell. As the COPI progress from the *cis* to *trans* Golgi, each time they bud off, uncoat, and fuse with the next cisterna their morphology is altered. The vesicle diameter, membrane thickness, cargo, all reflect the

characteristics of the parent Golgi membrane, whereas the vesicle coat itself remains structurally unchanged. These insights could not have been obtained from a reconstituted system alone. On the other hand, understanding the COPI architecture at the secondary-structure level was only possible from the *ex situ* COPI data and the integration of atomic details provided by crystallographic methods. This example illustrates how different levels of information can be meaningfully integrated to provide a comprehensive picture of a complex system.

## Poly-Gly-Ala aggregates in intact neurons

*In situ* cryo-ET of poly-Gly-Ala aggregates associated with amyotrophic lateral sclerosis and frontotemporal dementia provide an example of how alteration of the intracellular environment affects the local concentration of other molecular species [125]. CLEM was used to locate fluorescently tagged poly-Gly-Ala aggregates in transfected rat neurons and to target them for FIB-milling. Cryo-ET revealed networks of poly-Gly-Ala composed of polymorphic ribbons (Fig. 4C). The aggregates are densely populated with a single molecular species, the 26S proteasome. Compared with the surrounding cytosol, the concentration within the aggregate is increased ~30-fold. Given the local abundance of proteasomes, sub-tomograms with a resolution of ~10 Å could be generated and classification allowed to distinguish between conformations corresponding to the basic functional states: the ground state and the substrate-processing state [126]. Mapping these two conformations back into the tomograms of the segmented aggregate material showed that the proteasomes identified as being engaged with substrate are invariably in close contact with the poly-Gly-Ala ribbons. This suggests that they are engaged with the substrate, but fail to degrade it. Becoming stalled upon interaction with the aggregate material severely compromises the cellular protein quality control system.

## Challenges ahead

### From low throughput to higher throughput

The transition from electron tomography of resin-embedded and metal-stained cellular samples to low-dose imaging of vitrified specimens was enabled by automation of the data acquisition [127–129]. Since demonstrating the feasibility of cryo-ET [130], a workflow has been established that enables structural studies *in situ* to be performed with a wide range of cellular systems. However, throughput is still a limitation when

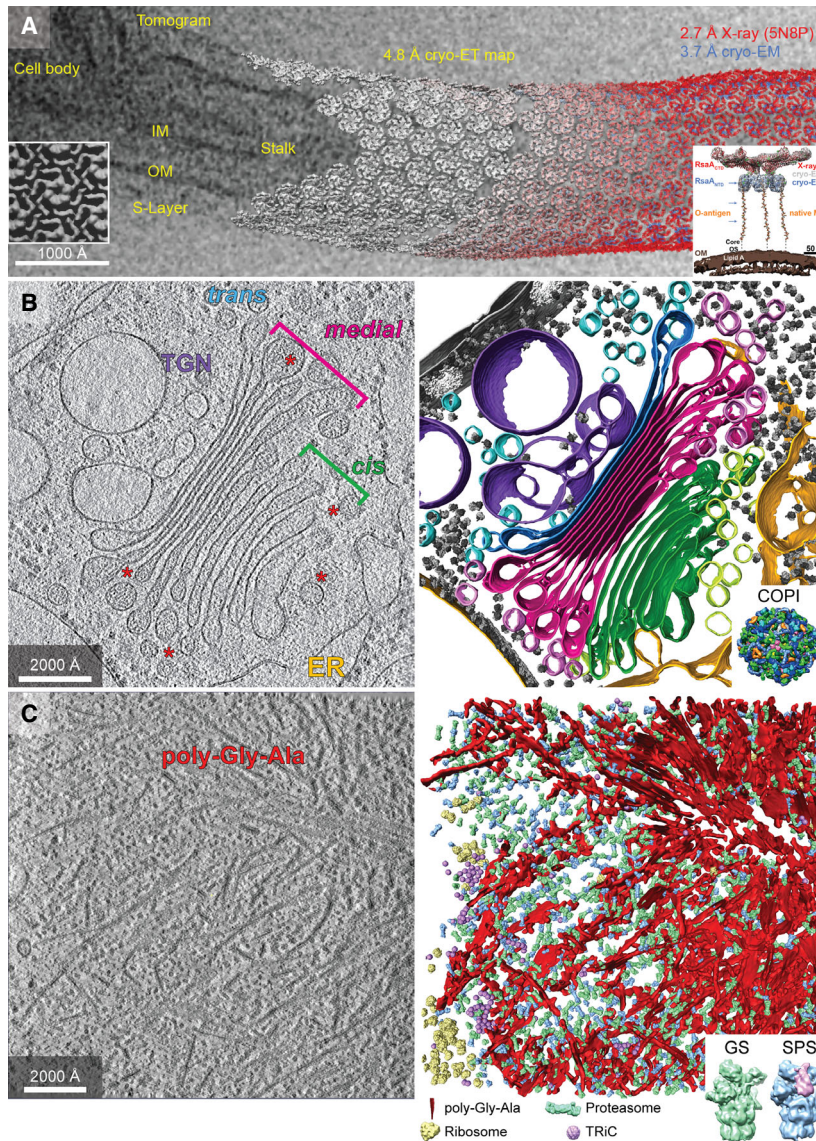


**Fig. 4.** Examples of *in situ* cryo-ET application. (A) Data integration from molecules to cells. A tomographic slice of a *C. crescentus* cell showing the inner membrane (IM), outer membrane (OM), and surface layers (S-layer). The 4.8 Å *in situ* cryo-ET sub-tomogram averages (gray) of the S-layer lattice are mapped back into the tomogram, and structures from X-ray crystallography at 2.7 Å (red) and single-particle averaging at 3.7 Å (blue) are docked. The inset (right) illustrates an integrative model of the S-layer anchoring into the outer membrane, combining structural and native MS methods. For comparison, the inset (left) shows an early electron crystallography map of the S-layer ring structure at 2 nm resolution [124]. (B) The *in situ* molecular organization of the Golgi apparatus from *C. reinhardtii*. A tomographic slice containing the cisternae stacks of the Golgi apparatus (left) and its segmented representation (right) revealing the cis (green), medial (magenta), and trans (blue) cisternae and COPI vesicles as well as the morphology of the endoplasmic reticulum (ER, yellow), trans Golgi network (TGN, purple), and two nuclear pore complexes, ribosomes, and other membranes (gray). In the tomographic slice, several COPI-coated vesicles and those budding off are indicated by asterisks. The inset shows the molecular architecture of the *ex situ* COPI-coated vesicle. (C) Molecular sociology within poly-Gly-Ala aggregates shows an increased concentration of 26S proteasomes. A tomographic slice (left) of a neuron expressing poly-Gly-Ala repeats. Mapping of macromolecules near the periphery of an aggregate region (right) shows 26S proteasomes in the ground state (GS, green) and an enrichment for the substrate-processing state (SPS, blue) proximal to poly-Gly-Ala twisted ribbons (red). Other molecular species, such as the ribosomes (yellow) and the chaperonin TRiC (purple), are largely excluded from the aggregate material. The inset shows a closeup of two 26S proteasome sub-tomogram averages after classification revealing the non-processing GS and the engaged SPS. Figure (A) inset (left) reproduced from Ref. [124].

large datasets are needed for quantitative analyses and for sub-tomogram classification and averaging. In single-particle analysis, purification of the molecules of interest results in a massive increase in concentration and the number of particles is almost never a limitation. In *in situ* cryo-ET, the natural abundance of a molecule in the cell determines the copy numbers per tomogram. Moreover, *in situ* a higher degree of heterogeneity may be encountered, as different functional and conformational states often coexist. Imaging of cellular samples has a considerable discovery potential for mapping macromolecular interactions, but often requires collecting more data than for purified specimens. For example, to perform the structural analysis of the COPI vesicles, 61 and 60 tomograms were collected for both *ex situ* and *in situ* datasets. However, the *in situ* dataset contained four times fewer copies of COPI, despite recording over an area twice as large. Another factor reducing the yield of *in situ* cryo-ET is often the lack of high-contrast intracellular fiducial markers. As a result, half of the *in situ* COPI tomograms had to be discarded due to unacceptable alignment errors resulting from variations in sample quality. To achieve a comparable *in situ* dataset would require the acquisition of ~ 250 tomograms even in a scenario where every tomogram would contain at least one Golgi apparatus.

This requires preparation of numerous lamellae using Ga<sup>+</sup> FIB-milling, which is currently a time-consuming manual process. For thicker specimens, the milling time scales in proportion with the amount of material that needs to be ablated. At the current throughput of typically 5–10 lamellae per day, the sample preparation is slower than the recording capabilities of TEMs. Many steps of the milling process are repetitive and have been automated in the material sciences; this is not yet common in cryo-FIB-milling [131]. All steps of the workflow, from data acquisition to data analysis will benefit from task automation wherever this is possible. While automation would provide some remedy, Ga<sup>+</sup> FIB-milling is intrinsically limited by low beam currents. Xe<sup>+</sup> plasma FIB offers faster sputtering rates and two orders of magnitude higher beam currents [132] and is a promising alternative. Together with an automated milling procedure preparation of up to 5 lamellae/ hour is now possible [133].

Thicker samples present additional challenges. First, vitrification of ~ 5 µm samples or beyond cannot be achieved by plunge freezing. High-pressure freezing devices are limited to ~ 150 µm thickness of material or alternatively up to a few hundred µm with double-sided cooling devices [22]. With microfluidic freezing

platforms, the sample thickness is given by the channel depth of 20 µm [32]. Freezing of bulk specimens has not seen substantial improvements in the past two or three decades and would need revisiting, to make tissue vitrification routine. Second, finding the region of interest in the block of ice and trimming it down requires a combination of cryo-fluorescence microscopy (FM), FIB-milling, and FIB lift-out. To enable precise 3D targeting of features of interest in an automated manner, such an approach requires the development of suitable models to incorporate the image information into deep learning approaches [134]. Correlating fluorescence and electron microscopy is relatively straightforward with thin samples. Correlation is aided by fiducial markers on the sample surface [135] and has recently become integrated into an automated workflow [131,136]. But this approach would need some adaptation for correlating features in larger frozen volumes.

Currently, the CLEM workflow requires the transfer of samples between specialized equipment for FM, FIB-milling, and finally TEM. Ice contamination is difficult to avoid during sample transfer. While being acceptable in the early sample preparation steps, after preparation of lamellae it should be avoided; even minor contaminations can affect data quality, while ice crystals obstruct the beam and reduce areas suitable for tomogram acquisition. Moreover, any sample deformations after FM affect the signal correlation. This can be problematic during the final stages of FIB-milling where bending of lamellae is not uncommon and often requires to stop the thinning process prematurely. Tension buildup resulting from large temperature changes during vitrification of materials with different expansion coefficients (carbon supports on metal grids) can be reduced by milling micro-expansion joints next to cells, but this can lead to displacement of the specimen and interfere with correlation [137]. Alternatively, all-gold supports do not suffer from different expansion coefficients, but their mechanical stability is much lower [138].

At the current resolution, FM is mainly used for targeting areas of interest and not for correlative interpretation. However, super-resolution FM correlative approaches have the potential to contribute to molecular identification. Increased fluorophore photostability at cryogenic temperatures can provide the needed photon counts for their precise localization also in samples considered too thick for EM. Recently, imaging inside a He-cooled cryostat enabled correlative super-resolution FIB-SEM to reveal identities of 100–200 nm large vesicles inside whole cells [7]. To fully harness the identification power of super-resolution methods it

would be advantageous to close the resolution gap down to  $\sim 30$  nm or below, which is already possible for fixated cells with interferometric photoactivated localization microscopy imaging [139]. For vitrified specimens localizing microtubule bundles inside human bone osteosarcoma epithelial cells (U2OS) is a recent achievement that required addressing the increased drift of cryostages and devitrification induced by the excitation laser [140].

Integrating FM and FIB-milling into one instrument would facilitate switching between different imaging modalities over different scales and eliminate the risk of contamination during sample transfer. Such an instrument would not only open up new possibilities for workflow optimization but would also help develop new strategies for dealing with thick specimens.

### Data acquisition speedup

The acquisition of tomographic data is considerably slower than data acquisition for single-particle cryo-EM. To acquire a tomogram with 41 projections around 32 min are required using the dose-symmetric tilt scheme [35], whereas anywhere between 100 and 200 micrographs can be recorded in the same time for single-particle analysis. Overhead time is spent on accurate focusing and tracking to compensate for the movement of the stage between tilting steps. In addition, the requirements for precise tracking and stage settling increase with magnification, leading to even longer acquisition times. New single-tilt axis holders reduce the stage settling time practically to zero and obviate the need for tracking. This considerably speeds up acquisition of a dose-symmetric tilt series to under 5 min, but the effect on high-resolution sub-tomogram averaging still needs further investigation [141]. Alternatively, piezoelectric-driven stages provide superior precision (14 pm) and ultra-low drift ( $11 \text{ pm}\cdot\text{s}^{-1}$ ), but they are not yet available commercially and would require some redesign of the current grids [142].

Setting up acquisition areas will also require automation to keep up with faster tomogram recording rates. Automated data acquisition of *in situ* samples is challenging, because of the high variability of lamellae content and could benefit from machine learning approaches. For *ex situ* samples the task is simpler, since the grid support raster can be used to target areas, similar to single-particle acquisition.

### Detection and classification of small particles

Identification of molecular complexes in complex *in situ* environments is challenging, because the

inventory of molecular species spans several orders of magnitude in size and abundance. For example, a commonly cultured human cell line is populated with over 10 000 different proteins ranging in copy numbers from anywhere below 500 to over 20 million copies per cell [143]. Attempting to find molecular complexes in a template-based approach would require the availability of comprehensive template libraries, but often templates do not exist. For an approach toward building a functional model of the whole cell, the number of available structural and homology models with a high sequence coverage was recently estimated for the pancreatic  $\beta$ -cell [144]. The estimates show that structures exist for 28% of the 11 700 estimated protein species and while these numbers may be discouraging for a template-based approach they suggest that there is considerable potential for template-free approaches. To achieve a complete structural and spatial representation of the cell's proteome, that is the goal of visual proteomics [145], further developments of pattern mining methods will be necessary [72,73,146]. However, with decreasing size of molecular species, it becomes increasingly difficult to detect particles in noisy tomograms and to reliably align and classify them. Thus, smaller and less abundant complexes may escape detection and analysis. The same applies to single-particle cryo-EM, which relies heavily on averaging to improve the resolution and SNR, just as sub-tomogram averaging does. In practice, however, single-particle cryo-EM reconstructions of  $< 100$  kDa proteins are possible [147], while molecular complexes smaller than 500 kDa are currently considered small for sub-tomogram averaging. To assess the detection rate of template matching by a scoring function, cryo-ET has been used in combination with quantitative MS in *Leptospira interrogans* [148].

One way to extend the lower-end size-limit in cryo-ET is to use a phase plate for contrast enhancement. Positioned at the diffraction plane, a phase plate converts the information imprinted on the phase of the electron wave into detectable amplitude modulation, by inducing a  $\pi/2$  phase shift between the unscattered electron wave relative to the scattered electron waves. This enables data collection close to focus and provides substantial contrast transfer at low spatial frequencies, which is advantageous for recognizing and aligning smaller objects. Despite the success of the Zernike phase plate (ZPP) in light microscopy, the precision required to manufacture analogous devices for TEM delayed the realization of early proposals by decades [149]. Higher contrast and similar resolution to conventional TEM were obtained with the thin-film ZPP [150]. However, the ZPP was impractical for

routine use, because of its short lifespan, it required precise centering of the hole, and automated data acquisition was not achieved [151]. Moreover, the central hole where the direct beam passes unaffected caused fringes in the images and its diameter determined the onset of the phase shift (cut-on periodicity). These problems were overcome with the Volta phase plate (VPP), which also uses a thin amorphous carbon film, but relies on the electron beam to induce the phase shift and offers a practical solution to many shortcomings of earlier designs [151,152]. Since there is no hole, the need for centering is obviated and the only requirement is the precise tuning of the TEM. The VPP regenerates over time and has a lifespan of years, if handled appropriately. More importantly, the VPP is compatible with automated data acquisition, and with software advances that included CTF phase fitting and correction, larger datasets could be acquired close to focus. This resulted in reconstructions of 20S proteasomes at 2.4 Å and enabled reconstructions of hemoglobin (64 kDa) at 3.2 Å [153,154]. At the theoretical lower-end size-limit for single-particle analysis, images and 2D class averages of myoglobin (17 kDa) showed the stunning improvement in contrast the VPP provides [154]. Recently, using the VPP in cryo-ET the 52 kDa streptavidin became visible, although no sub-tomogram averaging was attempted [155]. However, a problem of using the VPP for lamellae is charge buildup that causes local differences in phase contrast and limits its usability. An additional thin metal coating mitigates this problem and has provided impressive views of the nuclear periphery [156]. For *Dictyostelium* cells milled using a wedge geometry, beam-induced charging was not an issue. VPP imaging over the resulting thickness gradient revealed the detailed structure of actin networks and enabled tracing of branch structures within the actin waves also in ~ 300 nm thick regions [157]. The boost in contrast from the VPP can be a decisive advantage to resolve features of cellular structures that require imaging in thicker areas. However, for extensive sub-tomogram averaging aiming for achieving high resolution, the use of VPP brings additional challenges. For tomography tilt series acquired close to focus, VPP images render CTF fitting and correction difficult, limiting the attainable resolution to the first CTF zero. Nevertheless, the contrast enhancement is advantageous and often the only way to visualize small non-repetitive features in tomograms.

In a novel promising approach, phase shift can be generated by sufficiently strong laser fields, taking advantage of the ponderomotive force [158]. The laser phase plate does not suffer from signal loss inherent to

thin-film phase plates and provides a stable phase shift that is tunable on-demand. However, at the moment the laser field strength is able to induce a  $\pi/2$  phase shift of 80 keV electrons and further developments are needed before its use can be tested on 300 keV electrons commonly used in cryo-ET [159].

### The missing data problem

Distortions resulting from the missing information at higher tilts beyond 60° are a fundamental problem in cryo-ET [37]. One way to approach this is to fill the frequency space by averaging sub-tomograms of objects in different orientations [160]. Another possibility is to optimize the information content in one tomogram. Computationally it is possible to infer what the missing wedge data would be, but it is not possible to recover unobserved data [161]. Obtaining tomograms over the full angular range has been successful for small bacteria trapped in glass capillaries [162]. To extend the angular range, circular FIB-milling patterns could be used to make cylindrical specimens at the expense of a much reduced volume. However, to precisely align cylindrical specimens for tilt series acquisition would be challenging and might render this approach impractical.

Another challenge in cryo-ET is the low SNR of the recorded images resulting from the electron dose restrictions. In light of recent technological improvements in electron detection and software analysis, Peet *et al.* [163] set out to accurately estimate the optimal electron energy per induced radiation damage for cryo-EM. Their results confirm that the elastic cross-section contributing to signal in the TEM images increases proportionately faster than the inelastic cross-section contributing to radiation damage, and accurate measurements suggest that for thinner samples of up to 600 Å using lower energy electrons (100 keV) would result in up to 25% improvement in information extraction, if appropriate detectors existed. For tomography the ability to image thicker samples would be desirable, but there is a limited advantage of increasing the acceleration voltage. The gain in penetration depth from 100 to 300 kV is 2-fold, but increases only an additional 1.5-fold from 300 kV to 1.2 MV as it goes along with a steep increase in the equipment costs and a higher likelihood of knock-on damage [164]. Nevertheless, the suggested direction is interesting, because it challenges the paradigm, that the sample thickness should be adjusted for TEM imaging. With automated tuning of microscopes, it would become possible to switch between different acceleration voltages and adjust the microscope to the

specimen thickness to achieve optimal information transfer. The same authors also discuss the benefit of chromatic aberration (Cc) correction that would render inelastically scattered electrons usable for phase contrast and enable an overall increase in the SNR.

An idea put forward by Danev *et al.* [165] is to use defocus modulations to optimally extract sample information. Inserting a small electrostatic lens at the back focal plane would allow control and fast tuning of the defocus parameter during acquisition, which can be used as an optical dose-dependent filter that follows the gradual demise of high-resolution structural features. For tomography this would allow to more evenly fill the frequency space by combining close-to-focus high-resolution information with high-defocus information for more reliable CTF determination and tilt series alignment within one movie frame sequence.

Cryo-ET has the unique potential to bridge the gap between the cellular and molecular worlds. Ideally, it would provide structural information over large cellular volumes. But the quest for high-resolution cryo-ET is incompatible with imaged volume. Imaging at high magnifications comes at the cost of reducing the field of view and imaging thick samples results in low-quality data. Considering that optimal specimen thickness for 300 keV electrons is around 100 nm [163], such tomograms show a small fraction of the cellular volume. For example, a 100 nm thin lamella of a typical baker's yeast with a diameter of 5  $\mu\text{m}$  would contain  $\sim 0.22\%$  of its total volume, if imaged at 2.5  $\text{\AA}/\text{pixel}$  on a 4 k detector. Large assemblies, such as nuclear pore complexes or vesicles, might not even fit in their entirety into 100 nm thick slabs, compromising the benefits. Depending on the biological question being addressed, often a compromise to record over a larger volume and to accommodate the features of interest at the cost of resolution is advantageous. To ensure high-resolution snapshots of the cell's interior are representative of the cell's state and to avoid missing rare events of interest, requires acquisition of many tomograms. Considering the increasing throughput in tomogram acquisition it is not unreasonable to consider covering large areas in a tessellated cryo-ET approach, where tomograms would be *in silico* stitched together to represent the entire volume of thinned specimens. This means a 100-fold increase of the imaged area compared to a single tomogram for a 12 by 12  $\mu\text{m}$  lamella, using the same imaging conditions as above. While beam-induced structural changes will present a challenge for implementing this approach to cryo-ET, such approaches were already successfully applied to plastic-embedded sections of, for example, U2OS cells [166]. Although overlapping regions will have higher

electron exposures, the central parts of tomograms would retain the high-resolution information for sub-tomogram averaging.

While such ideas are exciting in theory, practical solutions have to be found.

## The promise of Cryo-ET

Cryo-ET has made great progress over the last decade, which is reflected by the increasing number of successful applications. It has provided accurate views of unperturbed cellular landscapes, revealing their native molecular organization. For a long time, studying isolated molecular complexes was the only possible way of obtaining structural information for a mechanistic understanding of their functions. However, technology advances in cryo-ET now enable *in situ* structural studies at 3–4 nm resolution and, when applying averaging methods, sub-nanometer resolutions can be achieved. We are just beginning to realize the potential of cryo-ET as a tool for studying macromolecular crowding. Phase transitions in lipid droplets can be already detected and attributed to different cellular states [167], but the information contained in tomograms, when properly calibrated, could be used for measuring systematically local density fluctuations inside cells. This holds the potential to detect phase separation phenomena and map regions that define membraneless organelles [168]. While in favorable cases cryo-ET can provide near-atomic resolution, even at nanometer resolution, the cellular environment offers a tremendous potential to discover unexpected scenarios. An increasing number of reports have revealed that macromolecules are organized into functional microcompartments at the nuclear pore basket [64] or the endoplasmic reticulum [65], highlighting the importance of *in situ* studies. However, the difficulty of *in situ* cryo-ET lies in mining the rich information contained in the tomograms. Cellular complexity presents a challenge to identify macromolecules when sub-tomogram averaging fails to provide the resolution for unambiguous identification. Integrative approaches have shown success where individual methods could not provide the full picture and helped generate pseudoatomic models of large assemblies such as the 26S proteasome [169] or the nuclear pore complex [170]. In proximity to the already mapped assemblies, interacting smaller proteins could be modeled based on distance constraints provided by cross-linking MS data. There is no reason to believe that the integrative modeling approach could not be expanded to tomograms. In fact, a tomogram spanning  $\sim 1 \mu\text{m}^2$  and up to a few hundred nm in thickness can provide a structural

framework to integrate functional data and for docking high-resolution atomic structures into their cellular context. In addition, integrating MS data allows cross-validating tomographic results. Quantitative MS has the possibility to provide the ground truth of protein copy numbers, which could be used to assess the number of detected complexes and those that escaped detection. On a larger scale, cryo-ET can itself be integrated into larger volumes provided by FIB-SEM to provide pictures of whole cells. There is still a lot of potential to improve the workflow of sample preservation, data recording, information extraction, quantitative interpretation, and finally data integration with other methods. Developments in instrumentation and image analysis will undoubtedly continue to push the boundaries forward. They will help advance our understanding of known structures and lead to the discovery of new structural patterns orchestrating cellular functions.

## Acknowledgements

We thank Vladan Lučić for valuable discussions and critical reading of the manuscript. We are grateful to Miroslava Schaffer for the cryo-FIB lift-out image, and to Ben Engel and Qiang Guo for providing the *in situ* tomography images. Open access funding enabled and organized by Projekt DEAL.

## References

- Baumeister W (2005) From proteomic inventory to architecture. *FEBS Lett* **579**, 933–937.
- Sali A, Glaeser R, Earnest T and Baumeister W (2003) From words to literature in structural proteomics. *Nature* **422**, 216–225.
- Alberts B (1998) The cell as a collection of protein machines: preparing the next generation of molecular biologists. *Cell* **92**, 291–294.
- Steven A, Baumeister W, Johnson LN and Perham RN (2016) *Molecular Biology of Assemblies and Machines*. New York, NY: Garland Science.
- Beck M and Baumeister W (2016) Cryo-electron tomography: can it reveal the molecular sociology of cells in atomic detail? *Trends Cell Biol* **26**, 825–837.
- Cheng Y (2015) Single-particle Cryo-EM at crystallographic resolution. *Cell* **161**, 450–457.
- Hoffman DP, Shtengel G, Xu CS, Campbell KR, Freeman M, Wang L, Milkie DE, Pasolli HA, Iyer N, Bogovic JA *et al.* (2020) Correlative three-dimensional super-resolution and block-face electron microscopy of whole vitreously frozen cells. *Science* **367**, eaaz5357.
- Lučić V, Rigort A and Baumeister W (2013) Cryo-electron tomography: the challenge of doing structural biology in situ. *J Cell Biol* **202**, 407–419.
- Grünewald K, Desai P, Winkler DC, Heymann JB, Belnap DM, Baumeister W and Steven AC (2003) Three-dimensional structure of herpes simplex virus from Cryo-electron tomography. *Science* **302**, 1396–1398.
- Wan W, Kolesnikova L, Clarke M, Koehler A, Noda T, Becker S and Briggs JAG (2017) Structure and assembly of the Ebola virus nucleocapsid. *Nature* **551**, 394–397.
- Mattei S, Glass B, Hagen WJH, Kräusslich H-G and Briggs JAG (2016) The structure and flexibility of conical HIV-1 capsids determined within intact virions. *Science* **354**, 1434–1437.
- Schur FKM, Obr M, Hagen WJH, Wan W, Jakobi AJ, Kirkpatrick JM, Sachse C, Kräusslich H-G and Briggs JAG (2016) An atomic model of HIV-1 capsid-SP1 reveals structures regulating assembly and maturation. *Science* **353**, 506–508.
- Nicastro D, Frangakis AS, Typke D and Baumeister W (2000) Cryo-electron tomography of neurospora mitochondria. *J Struct Biol* **129**, 48–56.
- Nicastro D, Schwartz C, Pierson J, Gaudette R, Porter ME and McIntosh JR (2006) The molecular architecture of axonemes revealed by cryoelectron tomography. *Science* **313**, 944–948.
- Medalia O, Beck M, Ecke M, Weber I, Neujahr R, Baumeister W and Gerisch G (2007) Organization of actin networks in intact filopodia. *Curr Biol* **17**, 79–84.
- Bui KH, Yagi T, Yamamoto R, Kamiya R and Ishikawa T (2012) Polarity and asymmetry in the arrangement of dynein and related structures in the Chlamydomonas axoneme. *J Cell Biol* **198**, 913–925.
- Oikonomou CM, Chang Y-W and Jensen GJ (2016) A new view into prokaryotic cell biology from electron cryotomography. *Nat Rev Microbiol* **14**, 205–220.
- Farley MM, Hu B, Margolin W and Liu J (2016) Minicells, back in fashion. *J Bacteriol* **198**, 1186–1195.
- Toro-Nahuelpan M, Zagoriy I, Senger F, Blanchoin L, Théry M and Mahamid J (2019) Tailoring cryo-electron microscopy grids by photo-micropatterning for in-cell structural studies. *Nat Methods* **17**, 50–54.
- Dubochet J, Adrian M, Chang J-J, Homo J-C, Lepault J, McDowell AW and Schultz P (1988) Cryo-electron microscopy of vitrified specimens. *Q Rev Biophys* **21**, 129–228.
- McDonald K, Schwarz H, Müller-Reichert T, Webb R, Buser C and Morphew M. (2010) Chapter 28 - “Tips and Tricks” for High-Pressure Freezing of Model Systems. In *Methods in Cell Biology* (Müller-Reichert T ed), pp. 671–693. Academic Press, San Diego, CA.
- Moor H (1987) Theory and practice of high pressure freezing. In *Cryotechniques in Biological Electron Microscopy* (Steinbrecht RA and Zierold K, eds), pp. 175–191. Springer, Berlin, Heidelberg.

- 23 Al-Amoudi A, Studer D and Dubochet J (2005) Cutting artefacts and cutting process in vitreous sections for cryo-electron microscopy. *J Struct Biol* **150**, 109–121.
- 24 Rigort A, Bäuerlein FJB, Villa E, Eibauer M, Laugks T, Baumeister W and Plitzko JM (2012) Focused ion beam micromachining of eukaryotic cells for cryoelectron tomography. *Proc Natl Acad Sci USA* **109**, 4449–4454.
- 25 Marko M, Hsieh C, Schalek R, Frank J and Mannella C (2007) Focused-ion-beam thinning of frozen-hydrated biological specimens for cryo-electron microscopy. *Nat Methods* **4**, 215–217.
- 26 Schaffer M, Pfeffer S, Mahamid J, Kleindiek S, Laugks T, Albert S, Engel BD, Rummel A, Smith AJ, Baumeister W *et al.* (2019) A cryo-FIB lift-out technique enables molecular-resolution cryo-ET within native *Caenorhabditis elegans* tissue. *Nat Methods* **16**, 757–762.
- 27 Rigort A, Villa E, Bäuerlein FJB, Engel BD and Plitzko JM (2012) Chapter 14 - Integrative approaches for cellular cryo-electron tomography: correlative imaging and focused ion beam micromachining. In *Methods in Cell Biology* (Müller-Reichert T and Verkade P, eds), pp. 259–281. Academic Press, Oxford.
- 28 Rigort A, Bäuerlein FJB, Leis A, Gruska M, Hoffmann C, Laugks T, Böhm U, Eibauer M, Gnaegi H, Baumeister W *et al.* (2010) Micromachining tools and correlative approaches for cellular cryo-electron tomography. *J Struct Biol* **172**, 169–179.
- 29 Sartori A, Gatz R, Beck F, Rigort A, Baumeister W and Plitzko JM (2007) Correlative microscopy: bridging the gap between fluorescence light microscopy and cryo-electron tomography. *J Struct Biol* **160**, 135–145.
- 30 Schwartz CL, Sarbash VI, Ataulakhanov FI, McIntosh JR and Nicastro D (2007) Cryo-fluorescence microscopy facilitates correlations between light and cryo-electron microscopy and reduces the rate of photobleaching. *J Microsc* **227**, 98–109.
- 31 Moser F, Pražák V, Mordhorst V, Andrade DM, Baker LA, Hagen C, Grünwald K and Kaufmann R (2019) Cryo-SOFI enabling low-dose super-resolution correlative light and electron cryo-microscopy. *Proc Natl Acad Sci USA* **116**, 4804–4809.
- 32 Fuest M, Schaffer M, Nocera GM, Galilea-Kleinsteuber RI, Messling J-E, Heymann M, Plitzko JM and Burg TP (2019) In situ microfluidic cryofixation for cryo focused ion beam milling and cryo electron tomography. *Sci Rep* **9**, 1–10.
- 33 Saxton WO, Baumeister W and Hahn M (1984) Three-dimensional reconstruction of imperfect two-dimensional crystals. *Ultramicroscopy* **13**, 57–70.
- 34 Hagen WJH, Wan W and Briggs JAG (2017) Implementation of a cryo-electron tomography tilt-scheme optimized for high resolution subtomogram averaging. *J Struct Biol* **197**, 191–198.
- 35 Turoňová B, Hagen WJH, Obr M, Mosalaganti S, Beugelink JW, Zimmerli CE, Kräusslich H-G and Beck M (2020) Benchmarking tomographic acquisition schemes for high-resolution structural biology. *Nat Commun* **11**, 1–9.
- 36 Glaeser RM (2016) Chapter two - specimen behavior in the electron beam. In *Methods in Enzymology* (Crowther RA, ed), pp. 19–50. Cambridge, MA: Academic Press.
- 37 Lučić V, Förster F and Baumeister W (2005) Structural studies by electron tomography: from cells to molecules. *Annu Rev Biochem* **74**, 833–865.
- 38 Penczek P, Marko M, Buttle K and Frank J (1995) Double-tilt electron tomography. *Ultramicroscopy* **60**, 393–410.
- 39 Shannon CE (1949) Communication in the presence of noise. *Proc IRE* **37**, 10–21.
- 40 Brilot AF, Chen JZ, Cheng A, Pan J, Harrison SC, Potter CS, Carragher B, Henderson R and Grigorieff N (2012) Beam-induced motion of vitrified specimen on holey carbon film. *J Struct Biol* **177**, 630–637.
- 41 Grant T and Grigorieff N (2015) Measuring the optimal exposure for single particle cryo-EM using a 2.6 Å reconstruction of rotavirus VP6. *eLife* **4**, e06980.
- 42 Fernandez J-J, Li S, Bharat TAM and Agard DA (2018) Cryo-tomography tilt-series alignment with consideration of the beam-induced sample motion. *J Struct Biol* **202**, 200–209.
- 43 Mastronarde DN and Held SR (2017) Automated tilt series alignment and tomographic reconstruction in IMOD. *J Struct Biol* **197**, 102–113.
- 44 Chen M, Bell JM, Shi X, Sun SY, Wang Z and Ludtke SJ (2019) A complete data processing workflow for cryo-ET and subtomogram averaging. *Nat Methods* **16**, 1161–1168.
- 45 Noble AJ and Stagg SM (2015) Automated batch fiducial-less tilt-series alignment in Appion using Protomo. *J Struct Biol* **192**, 270–278.
- 46 Mindell JA and Grigorieff N (2003) Accurate determination of local defocus and specimen tilt in electron microscopy. *J Struct Biol* **142**, 334–347.
- 47 Fernández JJ, Li S and Crowther RA (2006) CTF determination and correction in electron cryotomography. *Ultramicroscopy* **106**, 587–596.
- 48 Zanetti G, Riches JD, Fuller SD and Briggs JAG (2009) Contrast transfer function correction applied to cryo-electron tomography and sub-tomogram averaging. *J Struct Biol* **168**, 305–312.
- 49 Kunz M and Frangakis AS (2017) Three-dimensional CTF correction improves the resolution of electron tomograms. *J Struct Biol* **197**, 114–122.
- 50 Turoňová B, Schur FKM, Wan W and Briggs JAG (2017) Efficient 3D-CTF correction for cryo-electron

- tomography using NovaCTF improves subtomogram averaging resolution to 3.4Å. *J Struct Biol* **199**, 187–195.
- 51 Radermacher M (1992) Weighted back-projection methods. In *Electron Tomography: Three-Dimensional Imaging with the Transmission Electron Microscope* (Frank J, ed), pp. 91–115. Springer, Boston, MA.
- 52 Ramachandran GN and Lakshminarayanan AV (1971) Three-dimensional reconstruction from radiographs and electron micrographs: application of convolutions instead of fourier transforms. *Proc Natl Acad Sci USA* **68**, 2236–2240.
- 53 Wan W and Briggs JAG (2016) Chapter thirteen - Cryo-electron tomography and subtomogram averaging. In *Methods in Enzymology* (Crowther RA ed), pp. 329–367. Cambridge, MA: Academic Press.
- 54 Yan R, Venkatakrishnan SV, Liu J, Bouman CA and Jiang W (2019) MBIR: a cryo-ET 3D reconstruction method that effectively minimizes missing wedge artifacts and restores missing information. *J Struct Biol* **206**, 183–192.
- 55 Deng Y, Chen Y, Zhang Y, Wang S, Zhang F and Sun F (2016) ICON: 3D reconstruction with ‘missing-information’ restoration in biological electron tomography. *J Struct Biol* **195**, 100–112.
- 56 Chen Y and Förster F (2014) Iterative reconstruction of cryo-electron tomograms using nonuniform fast Fourier transforms. *J Struct Biol* **185**, 309–316.
- 57 Kunz M and Frangakis AS (2014) Super-sampling SART with ordered subsets. *J Struct Biol* **188**, 107–115.
- 58 Turoňová B, Marsalek L, Davidovič T and Slusallek P (2015) Progressive stochastic reconstruction technique (PSRT) for cryo electron tomography. *J Struct Biol* **189**, 195–206.
- 59 Frangakis AS and Hegerl R (2001) Noise reduction in electron tomographic reconstructions using nonlinear anisotropic diffusion. *J Struct Biol* **135**, 239–250.
- 60 Fernández J-J and Li S (2003) An improved algorithm for anisotropic nonlinear diffusion for denoising cryo-tomograms. *J Struct Biol* **144**, 152–161.
- 61 Rigort A, Günther D, Hegerl R, Baum D, Weber B, Prohaska S, Medalia O, Baumeister W and Hege H-C (2012) Automated segmentation of electron tomograms for a quantitative description of actin filament networks. *J Struct Biol* **177**, 135–144.
- 62 Martinez-Sanchez A, Garcia I, Asano S, Lucic V and Fernandez J-J (2014) Robust membrane detection based on tensor voting for electron tomography. *J Struct Biol* **186**, 49–61.
- 63 Buchholz T-O, Jordan M, Pigino G and Jug F (2019) Cryo-CARE: Content-Aware Image Restoration for Cryo-Transmission Electron Microscopy Data. In *2019 IEEE 16th International Symposium on Biomedical Imaging (ISBI 2019)*, pp. 502–506.
- 64 Albert S, Schaffer M, Beck F, Mosalaganti S, Asano S, Thomas HF, Plitzko JM, Beck M, Baumeister W and Engel BD (2017) Proteasomes tether to two distinct sites at the nuclear pore complex. *Proc Natl Acad Sci USA* **114**, 13726–13731.
- 65 Albert S, Wietrzynski W, Lee C-W, Schaffer M, Beck F, Schuller JM, Salomé PA, Plitzko JM, Baumeister W and Engel BD (2020) Direct visualization of degradation microcompartments at the ER membrane. *Proc Natl Acad Sci USA* **117**, 1069–1080.
- 66 Böhm J, Frangakis AS, Hegerl R, Nickell S, Typke D and Baumeister W (2000) Toward detecting and identifying macromolecules in a cellular context: template matching applied to electron tomograms. *Proc Natl Acad Sci USA* **97**, 14245–14250.
- 67 Frangakis AS, Böhm J, Förster F, Nickell S, Nicastro D, Typke D, Hegerl R and Baumeister W (2002) Identification of macromolecular complexes in cryoelectron tomograms of phantom cells. *Proc Natl Acad Sci USA* **99**, 14153–14158.
- 68 Kremer JR, Mastronarde DN and McIntosh JR (1996) Computer visualization of three-dimensional image data using IMOD. *J Struct Biol* **116**, 71–76.
- 69 Pruggnaller S, Mayr M and Frangakis AS (2008) A visualization and segmentation toolbox for electron microscopy. *J Struct Biol* **164**, 161–165.
- 70 Chen M, Dai W, Sun SY, Jonasch D, He CY, Schmid MF, Chiu W and Ludtke SJ (2017) Convolutional neural networks for automated annotation of cellular cryo-electron tomograms. *Nat Methods* **14**, 983–985.
- 71 Zeng X, Leung MR, Zeev-Ben-Mordehai T and Xu M (2018) A convolutional autoencoder approach for mining features in cellular electron cryo-tomograms and weakly supervised coarse segmentation. *J Struct Biol* **202**, 150–160.
- 72 Martinez-Sanchez A, Kochovski Z, Laugks U, Meyer Zum Alten Borgloh J, Chakraborty S, Pfeffer S, Baumeister W and Lučić V (2020) Template-free detection and classification of membrane-bound complexes in cryo-electron tomograms. *Nat Methods* **17**, 209–216.
- 73 Xu M, Tocheva EI, Chang Y-W, Jensen GJ and Alber F (2019) De novo visual proteomics in single cells through pattern mining. *Structure* **27**, 679–691.e14.
- 74 Scheres SHW and Chen S (2012) Prevention of overfitting in cryo-EM structure determination. *Nat Methods* **9**, 853–854.
- 75 Sigworth FJ (1998) A maximum-likelihood approach to single-particle image refinement. *J Struct Biol* **122**, 328–339.
- 76 Förster F, Pruggnaller S, Seybert A and Frangakis AS (2008) Classification of cryo-electron sub-tomograms using constrained correlation. *J Struct Biol* **161**, 276–286.

- 77 Bartesaghi A, Sprechmann P, Liu J, Randall G, Sapiro G and Subramaniam S (2008) Classification and 3D averaging with missing wedge correction in biological electron tomography. *J Struct Biol* **162**, 436–450.
- 78 Xu M and Alber F (2012) High precision alignment of cryo-electron subtomograms through gradient-based parallel optimization. *BMC Syst Biol* **6**, S18.
- 79 Scheres SHW, Melero R, Valle M and Carazo J-M (2009) Averaging of electron subtomograms and random conical tilt reconstructions through likelihood optimization. *Structure* **17**, 1563–1572.
- 80 Stölken M, Beck F, Haller T, Hegerl R, Gutsche I, Carazo J-M, Baumeister W, Scheres SHW and Nickell S (2011) Maximum likelihood based classification of electron tomographic data. *J Struct Biol* **173**, 77–85.
- 81 Yu Z and Frangakis AS (2011) Classification of electron sub-tomograms with neural networks and its application to template-matching. *J Struct Biol* **174**, 494–504.
- 82 Chen Y, Pfeffer S, Fernández JJ, Sorzano COS and Förster F (2014) Autofocused 3D classification of cryoelectron subtomograms. *Structure* **22**, 1528–1537.
- 83 Asano S, Fukuda Y, Beck F, Aufderheide A, Förster F, Danev R and Baumeister W (2015) A molecular census of 26S proteasomes in intact neurons. *Science* **347**, 439–442.
- 84 Fukuda Y, Beck F, Plitzko JM and Baumeister W (2017) In situ structural studies of tripeptidyl peptidase II (TPPII) reveal spatial association with proteasomes. *Proc Natl Acad Sci USA* **114**, 4412–4417.
- 85 Castaño-Díez D (2017) The Dynamo package for tomography and subtomogram averaging: components for MATLAB, GPU computing and EC2 Amazon Web Services. *Acta Crystallogr Struct Biol* **73**, 478–487.
- 86 Galaz-Montoya JG, Flanagan J, Schmid MF and Ludtke SJ (2015) Single particle tomography in EMAN2. *J Struct Biol* **190**, 279–290.
- 87 Himes BA and Zhang P (2018) emClarity: software for high-resolution cryo-electron tomography and subtomogram averaging. *Nat Methods* **15**, 955–961.
- 88 Heumann JM, Hoenger A and Mastrorade DN (2011) Clustering and variance maps for cryo-electron tomography using wedge-masked differences. *J Struct Biol* **175**, 288–299.
- 89 Winkler H (2007) 3D reconstruction and processing of volumetric data in cryo-electron tomography. *J Struct Biol* **157**, 126–137.
- 90 Hrabe T, Chen Y, Pfeffer S, Kuhn Cuellar L, Mangold A-V and Förster F (2012) PyTom: a python-based toolbox for localization of macromolecules in cryo-electron tomograms and subtomogram analysis. *J Struct Biol* **178**, 177–188.
- 91 Bharat TAM and Scheres SHW (2016) Resolving macromolecular structures from electron cryo-tomography data using subtomogram averaging in RELION. *Nat Protoc* **11**, 2054–2065.
- 92 Förster F, Medalia O, Zauberman N, Baumeister W and Fass D (2005) Retrovirus envelope protein complex structure in situ studied by cryo-electron tomography. *Proc Natl Acad Sci USA* **102**, 4729–4734.
- 93 Qu K, Glass B, Doležal M, Schur FKM, Murciano B, Rein A, Rumlová M, Ruml T, Kräusslich H-G and Briggs JAG (2018) Structure and architecture of immature and mature murine leukemia virus capsids. *Proc Natl Acad Sci USA* **115**, E11751–E11760.
- 94 Prasad VM, Klose T and Rossmann MG (2017) Assembly, maturation and three-dimensional helical structure of the teratogenic rubella virus. *PLOS Pathog* **13**, e1006377.
- 95 Zeev-Ben-Mordehai T, Vasishtan D, Durán AH, Vollmer B, White P, Pandurangan AP, Siebert CA, Topf M and Grünewald K (2016) Two distinct trimeric conformations of natively membrane-anchored full-length herpes simplex virus 1 glycoprotein B. *Proc Natl Acad Sci USA* **113**, 4176–4181.
- 96 Turoňová B, Sikora M, Schürmann C, Hagen WJH, Welsch S, Blanc FEC, von Bülow S, Gecht M, Bagola K, Hörner C *et al.* (2020) In situ structural analysis of SARS-CoV-2 spike reveals flexibility mediated by three hinges. *Science* **370** (6513), 203–208.
- 97 Ke Z, Oton J, Qu K, Cortese M, Zila V, McKeane L, Nakane T, Zivanov J, Neufeldt CJ, Cerikan B *et al.* (2020) Structures and distributions of SARS-CoV-2 spike proteins on intact virions. *Nature*.
- 98 Beck M, Förster F, Ecke M, Plitzko JM, Melchior F, Gerisch G, Baumeister W and Medalia O (2004) Nuclear pore complex structure and dynamics revealed by cryoelectron tomography. *Science* **306**, 1387–1390.
- 99 von Appen A, Kosinski J, Sparks L, Ori A, DiGuilio AL, Vollmer B, Mackmull M-T, Banterle N, Parca L, Kastrius P *et al.* (2015) In situ structural analysis of the human nuclear pore complex. *Nature* **526**, 140–143.
- 100 Zhang Y, Li S, Zeng C, Huang G, Zhu X, Wang Q, Wang K, Zhou Q, Yan C, Zhang W *et al.* (2020) Molecular architecture of the luminal ring of the *Xenopus laevis* nuclear pore complex. *Cell Res* **30**, 532–540.
- 101 O'Reilly FJ, Xue L, Graziadei A, Sinn L, Lenz S, Tegunov D, Blötz C, Singh N, Hagen WJH, Cramer P *et al.* (2020) In-cell architecture of an actively transcribing-translating expressome. *Science* **369**, 554–557.
- 102 Pfeffer S, Dudek J, Schaffer M, Ng BG, Albert S, Plitzko JM, Baumeister W, Zimmermann R, Freeze HH, Engel BD *et al.* (2017) Dissecting the molecular organization of the translocon-associated protein complex. *Nat Commun* **8**, 1–9.
- 103 Braunger K, Pfeffer S, Shrimal S, Gilmore R, Berninghausen O, Mandon EC, Becker T, Förster F

- and Beckmann R (2018) Structural basis for coupling protein transport and N-glycosylation at the mammalian endoplasmic reticulum. *Science* **360**, 215–219.
- 104 Faini M, Prinz S, Beck R, Schorb M, Riches JD, Bacia K, Brügger B, Wieland FT and Briggs JAG (2012) The structures of COPI-coated vesicles reveal alternate coatomer conformations and interactions. *Science* **336**, 1451–1454.
- 105 Dodonova SO, Diestelkoetter-Bachert P, von Appen A, Hagen WJH, Beck R, Beck M, Wieland F and Briggs JAG (2015) A structure of the COPI coat and the role of coat proteins in membrane vesicle assembly. *Science* **349**, 195–198.
- 106 Dodonova SO, Aderhold P, Kopp J, Ganeva I, Röhling S, Hagen WJH, Sinning I, Wieland F and Briggs JAG (2017) 9Å structure of the COPI coat reveals that the Arf1 GTPase occupies two contrasting molecular environments. *eLife* **6**, e26691.
- 107 Bykov YS, Schaffer M, Dodonova SO, Albert S, Plitzko JM, Baumeister W, Engel BD and Briggs JAG (2017) The structure of the COPI coat determined within the cell. *eLife* **6**, e32493.
- 108 Kovtun O, Leneva N, Bykov YS, Ariotti N, Teasdale RD, Schaffer M, Engel BD, Owen DJ, Briggs JAG and Collins BM (2018) Structure of the membrane-assembled retromer coat determined by cryo-electron tomography. *Nature* **561**, 561–564.
- 109 Kovtun O, Dickson VK, Kelly BT, Owen DJ and Briggs JAG (2020) Architecture of the AP2/clathrin coat on the membranes of clathrin-coated vesicles. *Sci Adv* **6**, eaba8381.
- 110 Cai S, Böck D, Pilhofer M and Gan L (2018) The in situ structures of mono-, di-, and trinucleosomes in human heterochromatin. *Mol Biol Cell* **29**, 2450–2457.
- 111 Sorrentino S, Studt J-D, Horev MB, Medalia O and Sapra KT (2016) Toward correlating structure and mechanics of platelets. *Cell Adhes Migr* **10**, 568–575.
- 112 Watanabe R, Buschauer R, Böhning J, Audagnotto M, Lasker K, Lu T-W, Boassa D, Taylor S and Villa E (2020) The in situ structure of Parkinson's disease-linked LRRK2. *Cell* **182**, 1508–1518.e16.
- 113 Guennec ML, Klena N, Gambarotto D, Laporte MH, Tassin A-M, van den Hoek H, Erdmann PS, Schaffer M, Kovacik L, Borgers S *et al.* (2020) A helical inner scaffold provides a structural basis for centriole cohesion. *Sci Adv* **6**, eaaz4137.
- 114 Böck D, Medeiros JM, Tsao H-F, Penz T, Weiss GL, Aistleitner K, Horn M and Pilhofer M (2017) In situ architecture, function, and evolution of a contractile injection system. *Science* **357**, 713–717.
- 115 Park D, Lara-Tejero M, Waxham MN, Li W, Hu B, Galán JE and Liu J (2018) Visualization of the type III secretion mediated Salmonella–host cell interface using cryo-electron tomography. *eLife* **7**, e39514.
- 116 Ghosal D, Kim KW, Zheng H, Kaplan M, Truchan HK, Lopez AE, McIntire IE, Vogel JP, Cianciotto NP and Jensen GJ (2019) *In vivo* structure of the Legionella type II secretion system by electron cryotomography. *Nat Microbiol* **4**, 2101–2108.
- 117 Rapisarda C, Cherrak Y, Kooger R, Schmidt V, Pellarin R, Logger L, Cascales E, Pilhofer M, Durand E and Fronzes R (2019) In situ and high-resolution cryo-EM structure of a bacterial type VI secretion system membrane complex. *EMBO J* **38**, e100886.
- 118 Cassidy CK, Himes BA, Sun D, Ma J, Zhao G, Parkinson JS, Stansfeld PJ, Luthey-Schulten Z and Zhang P (2020) Structure and dynamics of the *E. coli* chemotaxis core signaling complex by cryo-electron tomography and molecular simulations. *Commun Biol* **3**, 24.
- 119 Yang W, Cassidy CK, Ames P, Diebold CA, Schulten K, Luthey-Schulten Z, Parkinson JS and Briegel A (2019) In situ conformational changes of the *Escherichia coli* serine chemoreceptor in different signaling states. *MBio* **10**(4), e00973–19.
- 120 Chang Y, Zhang K, Carroll BL, Zhao X, Charon NW, Norris SJ, Motaleb MA, Li C and Liu J (2020) Molecular mechanism for rotational switching of the bacterial flagellar motor. *Nat Struct Mol Biol*.
- 121 von Kügelgen A, Tang H, Hardy GG, Kureisaite-Ciziene D, Brun YV, Stansfeld PJ, Robinson CV and Bharat TAM (2020) In Situ structure of an intact lipopolysaccharide-bound bacterial surface layer. *Cell* **180**, 348–358.e15.
- 122 D'Imprima E, Floris D, Joppe M, Sánchez R, Grininger M and Kühlbrandt W (2019) Protein denaturation at the air-water interface and how to prevent it. *eLife* **8**, e42747.
- 123 De Rosier DJ and Klug A (1968) Reconstruction of three dimensional structures from electron micrographs. *Nature* **217**, 130–134.
- 124 Smit J, Engelhardt H, Volker S, Smith SH and Baumeister W (1992) The S-layer of *Caulobacter crescentus*: three-dimensional image reconstruction and structure analysis by electron microscopy. *J Bacteriol* **174**, 6527–6538.
- 125 Guo Q, Lehmer C, Martínez-Sánchez A, Rudack T, Beck F, Hartmann H, Pérez-Berlanga M, Frottin F, Hipp MS, Hartl FU *et al.* (2018) In situ structure of neuronal C9orf72 Poly-GA aggregates reveals proteasome recruitment. *Cell* **172**, 696–705.
- 126 Wehmer M, Rudack T, Beck F, Aufderheide A, Pfeifer G, Plitzko JM, Förster F, Schulten K, Baumeister W and Sakata E (2017) Structural insights into the functional cycle of the ATPase module of the 26S proteasome. *Proc Natl Acad Sci USA* **114**, 1305–1310.
- 127 Dierksen K, Typke D, Hegerl R, Koster AJ and Baumeister W (1992) Towards automatic electron tomography. *Ultramicroscopy* **40**, 71–87.

- 128 Dierksen K, Typke D, Hegerl R and Baumeister W (1993) Towards automatic electron tomography II. Implementation of autofocus and low-dose procedures. *Ultramicroscopy* **49**, 109–120.
- 129 Koster AJ, Chen H, Sedat JW and Agard DA (1992) Automated microscopy for electron tomography. *Ultramicroscopy* **46**, 207–227.
- 130 Dierksen K, Typke D, Hegerl R, Walz J, Sackmann E and Baumeister W (1995) Three-dimensional structure of lipid vesicles embedded in vitreous ice and investigated by automated electron tomography. *Biophys J* **68**, 1416–1422.
- 131 Zachs T, Schertel A, Medeiros J, Weiss GL, Hugener J, Matos J and Pilhofer M (2020) Fully automated, sequential focused ion beam milling for cryo-electron tomography. *eLife* **9**, e52286.
- 132 Smith AD, Donoghue J, Garner A, Winiarski B, Bousser E, Carr J, Behnsen J, Burnett TL, Wheeler R, Wilford K *et al.* (2019) On the application of Xe<sup>+</sup> Plasma FIB for micro-fabrication of small-scale tensile specimens. *Exp Mech* **59**, 1113–1125.
- 133 Buckley G, Gervinskis G, Taveneau C, Venugopal H, Whisstock JC and de Marco A (2020) Automated cryo-lamella preparation for high-throughput in-situ structural biology. *J Struct Biol* **210**, 107488.
- 134 Withers PJ and Burnett TL (2019) Rich multi-dimensional correlative imaging. *IOP Conf Ser Mater Sci Eng* **580**, 012014.
- 135 Arnold J, Mahamid J, Lucic V, de Marco A, Fernandez J-J, Laugks T, Mayer T, Hyman AA, Baumeister W and Plitzko JM (2016) Site-specific cryo-focused ion beam sample preparation guided by 3D correlative microscopy. *Biophys J* **110**, 860–869.
- 136 Fu X, Ning J, Zhong Z, Ambrose Z, Watkins SC and Zhang P (2019) AutoCLEM: an automated workflow for correlative live-cell fluorescence microscopy and cryo-electron tomography. *Sci Rep* **9**, 1–10.
- 137 Wolff G, Limpens RWAL, Zheng S, Snijder EJ, Agard DA, Koster AJ and Bárcena M (2019) Mind the gap: micro-expansion joints drastically decrease the bending of FIB-milled cryo-lamellae. *J Struct Biol* **208**, 107389.
- 138 Russo CJ and Passmore LA (2016) Ultrastable gold substrates: properties of a support for high-resolution electron cryomicroscopy of biological specimens. *J Struct Biol* **193**, 33–44.
- 139 Shtengel G, Galbraith JA, Galbraith CG, Lippincott-Schwartz J, Gillette JM, Manley S, Sougrat R, Waterman CM, Kanchanawong P, Davidson MW *et al.* (2009) Interferometric fluorescent super-resolution microscopy resolves 3D cellular ultrastructure. *Proc Natl Acad Sci USA* **106**, 3125–3130.
- 140 Tuijtel MW, Koster AJ, Jakobs S, Faas FGA and Sharp TH (2019) Correlative cryo super-resolution light and electron microscopy on mammalian cells using fluorescent proteins. *Sci Rep* **9**, 1–11.
- 141 Chreifi G, Chen S, Metskas LA, Kaplan M and Jensen GJ (2019) Rapid tilt-series acquisition for electron cryotomography. *J Struct Biol* **205**, 163–169.
- 142 Ercius P, Boese M, Duden T and Dahmen U (2012) Operation of TEAM I in a user environment at NCEM. *Microsc Microanal* **18**, 676–683.
- 143 Beck M, Schmidt A, Malmstroem J, Claassen M, Ori A, Szymborska A, Herzog F, Rinner O, Ellenberg J and Aebersold R (2011) The quantitative proteome of a human cell line. *Mol Syst Biol* **7**, 549.
- 144 Singla J, McClary KM, White KL, Alber F, Sali A and Stevens RC (2018) Opportunities and challenges in building a spatiotemporal multi-scale model of the human pancreatic  $\beta$  cell. *Cell* **173**, 11–19.
- 145 Nickell S, Kofler C, Leis AP and Baumeister W (2006) A visual approach to proteomics. *Nat Rev Mol Cell Biol* **7**, 225–230.
- 146 Xu M, Beck M and Alber F (2011) Template-free detection of macromolecular complexes in cryo electron tomograms. *Bioinformatics* **27**, i69–i76.
- 147 Herzik MA, Wu M and Lander GC (2019) High-resolution structure determination of sub-100 kDa complexes using conventional cryo-EM. *Nat Commun* **10**, 1032.
- 148 Beck M, Malmström JA, Lange V, Schmidt A, Deutsch EW and Aebersold R (2009) Visual proteomics of the human pathogen *Leptospira interrogans*. *Nat Methods* **6**, 817–823.
- 149 Boersch H (1947) Über die Kontraste von Atomen im Elektronenmikroskop. *Z Für Naturforschung A* **2**, 615–633.
- 150 Danev R and Nagayama K (2001) Transmission electron microscopy with Zernike phase plate. *Ultramicroscopy* **88**, 243–252.
- 151 Danev R and Baumeister W (2017) Expanding the boundaries of cryo-EM with phase plates. *Curr Opin Struct Biol* **46**, 87–94.
- 152 Danev R, Buijsse B, Khoshouei M, Plitzko JM and Baumeister W (2014) Volta potential phase plate for in-focus phase contrast transmission electron microscopy. *Proc Natl Acad Sci USA* **111**, 15635–15640.
- 153 Danev R, Tegunov D and Baumeister W (2017) Using the Volta phase plate with defocus for cryo-EM single particle analysis. *eLife* **6**, e23006.
- 154 Khoshouei M, Danev R, Plitzko JM and Baumeister W (2017) Revisiting the structure of hemoglobin and myoglobin with cryo-electron microscopy. *J Mol Biol* **429**, 2611–2618.
- 155 Fan X, Wang J, Zhang X, Yang Z, Zhang J-C, Zhao L, Peng H-L, Lei J and Wang H-W (2019) Single particle cryo-EM reconstruction of 52 kDa streptavidin at 3.2 Angstrom resolution. *Nat Commun* **10**, 1–11.

- 156 Mahamid J, Pfeffer S, Schaffer M, Villa E, Danev R, Cuellar LK, Förster F, Hyman AA, Plitzko JM and Baumeister W (2016) Visualizing the molecular sociology at the HeLa cell nuclear periphery. *Science* **351**, 969–972.
- 157 Jasnin M, Beck F, Ecke M, Fukuda Y, Martinez-Sanchez A, Baumeister W and Gerisch G (2019) The architecture of traveling actin waves revealed by cryo-electron tomography. *Structure* **27**, 1211–1223.e5.
- 158 Müller H, Jin J, Danev R, Spence J, Padmore H and Glaeser RM (2010) Design of an electron microscope phase plate using a focused continuous-wave laser. *New J Phys* **12**, 073011.
- 159 Schwartz O, Axelrod JJ, Campbell SL, Turnbaugh C, Glaeser RM and Müller H (2019) Laser phase plate for transmission electron microscopy. *Nat Methods* **16**, 1016–1020.
- 160 Förster F and Hegerl R (2007) Structure determination in situ by averaging of tomograms. In *Methods in Cell Biology* (McIntoshJR, ed), pp. 741–767. Cambridge, MA: Academic Press.
- 161 Moebel E and Kervrann C (2020) A Monte Carlo framework for missing wedge restoration and noise removal in cryo-electron tomography. *J Struct Biol X* **4**, 100013.
- 162 Palmer CM and Löwe J (2014) A cylindrical specimen holder for electron cryo-tomography. *Ultramicroscopy* **137**, 20–29.
- 163 Peet MJ, Henderson R and Russo CJ (2019) The energy dependence of contrast and damage in electron cryomicroscopy of biological molecules. *Ultramicroscopy* **203**, 125–131.
- 164 Koster AJ, Grimm R, Typke D, Hegerl R, Stoschek A, Walz J and Baumeister W (1997) Perspectives of molecular and cellular electron tomography. *J Struct Biol* **120**, 276–308.
- 165 Danev R, Iijima H, Matsuzaki M and Motoki S (2020) Fast and accurate defocus modulation for improved tunability of cryo-EM experiments. *IUCrJ* **7**, 566–574.
- 166 O’Toole E, van der Heide P, Richard McIntosh J and Mastronarde D (2018) Large-scale electron tomography of cells using SerialEM and IMOD. In *Cellular Imaging: Electron Tomography and Related Techniques* (Hanssen E, ed), pp. 95–116. Springer International Publishing, Cham.
- 167 Mahamid J, Tegunov D, Maiser A, Arnold J, Leonhardt H, Plitzko JM and Baumeister W (2019) Liquid-crystalline phase transitions in lipid droplets are related to cellular states and specific organelle association. *Proc Natl Acad Sci USA* **116**, 16866–16871.
- 168 Hyman AA, Weber CA and Jülicher F (2014) Liquid-liquid phase separation in biology. *Annu Rev Cell Dev Biol* **30**, 39–58.
- 169 Lasker K, Förster F, Bohn S, Walzthoeni T, Villa E, Unverdorben P, Beck F, Aebersold R, Sali A and Baumeister W (2012) Molecular architecture of the 26S proteasome holocomplex determined by an integrative approach. *Proc Natl Acad Sci USA* **109**, 1380–1387.
- 170 Kim SJ, Fernandez-Martinez J, Nudelman I, Shi Y, Zhang W, Raveh B, Herricks T, Slaughter BD, Hogan JA, Upla P *et al.* (2018) Integrative structure and functional anatomy of a nuclear pore complex. *Nature* **555**, 475–482.